PNAS RESEARCH ARTICLE | BIOCHEMISTRY OPEN ACCESS

Structural basis of transition from initiation to elongation in de novo viral RNA-dependent RNA polymerases

Jiqin Wu[a,1], Xinyu Wang[a,b,1], Qiaojie Liu[a], Guoliang Lu[a,2], and Peng Gong[a,c,d,3]

Edited by Michael Summers, Department of Chemistry and Biochemistry, University of Maryland, Baltimore, MD; received July 5, 2022; accepted November 13, 2022

De novo viral RNA-dependent RNA polymerases (RdRPs) utilize their priming element (PE) to facilitate accurate initiation. Upon transition to elongation, the PE has to retreat from the active site to give room to the template–product RNA duplex. However, PE conformational change upon this transition and the role of PE at elongation both remain elusive. Here, we report crystal structures of RdRP elongation complex (EC) from dengue virus serotype 2 (DENV2), demonstrating a dramatic refolding of PE that allows establishment of interactions with the RNA duplex backbone approved to be essential for EC stability. Enzymology data from both DENV2 and hepatitis C virus (HCV) RdRPs suggest that critical transition of the refolding likely occurs after synthesis of a 4- to 5-nucleotide (nt) product together providing a key basis in understanding viral RdRP transition from initiation to elongation.

RNA virus | dengue virus | RNA-dependent RNA polymerase | de novo initiation | elongation complex

Significance

Viral RNA-dependent RNA polymerase (RdRP) carries out RNA synthesis through two modes of initiation: primer dependent and de novo. De novo RdRPs such as those from the family *Flaviviridae* utilize a priming element (PE) in their thumb domain to facilitate initiation. At initiation, PE reaches the active site and occupies the normal primer/product binding path. Upon transition to elongation, PE has to make room for the RNA duplex, but what PE does at elongation remains unresolved. Here, we report dengue virus RdRP elongation complex (EC) structures and demonstrate how PE refolds upon transition to elongation and establishes interactions with the RNA backbone to stabilize the EC, thus providing a molecular basis to this key process during RNA virus replication.

RNA-dependent RNA polymerases (RdRPs) encoded by RNA viruses are a unique class of nucleic acid polymerases that employ DNA-free replication and transcription and are key enzyme machineries to the understanding of RNA viruses and to develop antiviral strategies (1, 2). The RdRP catalytic core module adopts a signature encircled human right-hand architecture with the palm, fingers, and thumb domains surrounding the active site and fingertips–thumb interactions to make the encirclement (3, 4). Likely related to the encircled nature of their structures, RdRPs utilize a palm domain-based conformational change to close the active site for the chemistry step of the phosphoryl transfer reaction (5), while rotational movement of the fingers domain is common in active site closure by other classes of single-subunit polymerases (6–8). Another unique feature, although not in all RdRPs, is the utilization of a priming element (PE) often embedded in the RdRP thumb domain to achieve de novo initiation of RNA synthesis (4, 9). Among them, RdRPs from *Flaviviridae* and *Cystoviridae* are classical examples that solely use de novo mechanism. Crystal structures of initiation complexes (ICs) have been reported in hepatitis C virus (HCV, *Flaviviridae*) and bacteriophage phi6 (*Cystoviridae*) together providing a general basis of how PE interacts with the 3′-end of the template RNA and the initiating nucleoside triphosphates (NTPs) (a dinucleotide and an nucleoside diphosphate (NDP) in the HCV structure) (10, 11). Although PEs from different viral families exhibit diverse structures and sometimes comprise multiple peptide segments (10, 12, 13), they consistently form a "platform" with a flat-shaped hydrophobic tip stacking on the initiating nucleotide pairs based on the IC structures. However, the initiation-competent PE conformation is incompatible with an elongation complex (EC) containing a fully duplexed template–product RNA. How these PEs undergo conformational change upon transition to elongation and whether they play a role at the elongation phase both remain elusive primarily owing to the lack of classical de novo RdRP EC structures.

Flaviviridae members belong to positive-strand RNA viruses, and their RdRP proteins exhibit diversity in both global architecture and PE substructure. While the *Hepacivirus* HCV NS5B protein largely comprises the RdRP catalytic module, the *Pestivirus* classical swine fever virus (CSFV) NS5B and the *Flavivirus* dengue virus (DENV)/Japanese encephalitis virus (JEV) NS5 are natural fusions of RdRP and an N-terminal domain (NTD) or a methyltransferase (MTase), respectively (4, 13–16). Both HCV and CSFV RdRPs contain two-segment PEs with β-type structures, while DENV/JEV NS5 has a one-segment PE as a long loop insertion between two thumb domain helices. The flavivirus PE contains only 23 residues (e.g., residues 785 to 807 and 790 to 812 in DENV serotype 2 (DENV2) and JEV NS5, respectively) and is the structurally most simplified PE in known RdRP structures. In apo RdRP structures, PEs of HCV and DENV/JEV reach the active site. In the HCV IC structures, the C-terminal segment of PE (PE_C) retreats from the active site, while the N-terminal part (PE_N, a β-hairpin and the thumb insertion homologue of

Author contributions: P.G. designed research; J.W., X.W., and Q.L. performed research; J.W., X.W., G.L., and P.G. analyzed data; and J.W., X.W., G.L., and P.G. wrote the paper.

The authors declare no competing interest.

This article is a PNAS Direct Submission.

[1]J.W. and X.W. contributed equally to this work.

[2]Present address: State Key Laboratory of Genetic Engineering, School of Life Sciences, Fudan University, Shanghai 200438, China.

[3]To whom correspondence may be addressed. Email: gongpeng@wh.iov.cn.

This article contains supporting information online at https://www.pnas.org/lookup/suppl/doi:10.1073/pnas.2211425120/-/DCSupplemental.

Published December 28, 2022.

DENV/JEV PE) makes the stacking interactions with the initiating nucleotides. By contrast, the *Pestivirus* PE appears not long enough to reach the active site in apo RdRP structures (12, 14, 17), and functional data suggest that an induced-fit mechanism may exist with a PE conformational change for initiation upon binding of template RNA and initiating NTPs (17). The observed dynamic behaviors of *Flaviviridae* PEs are also consistent with their anticipated conformational changes during RdRP transition to elongation. However, whether they undergo rigid body mode movement or refolding or become disordered during the transition is of particular interest.

Building on successful assembly of RdRP EC of HCV, CSFV, and DENV (14, 18, 19), here we report two crystal structures of DENV2 RdRP EC that reveal a refolded PE with established interactions with the backbone of both RNA strands of the upstream duplex. Mutations critical to the PE refolding or at these interaction sites do not affect RdRP elongation rate but can reduce EC stability, while some EC stability–impaired mutants exhibit enhanced initiation efficiency. Enzymology characterization further suggests that critical transition toward elongation may occur after synthesis of a 4- to 5-nt product in both DENV2 and HCV RdRPs. These studies together demonstrate that PE is bifunctional and is probably optimized to balance RdRP initiation and elongation activities.

Results

Architecture of the DENV2 RdRP EC. With an aim to solve the structure of a classical de novo RdRP EC, we established CSFV and DENV2 EC assembly methodologies mainly based on previously reported approaches in HCV RdRP EC assembly and primer-dependent picornavirus RdRP EC assembly and structure determination (5, 14, 18–20). A 30-nt RNA template (T30) and a dinucleotide primer (P2) were used to assemble a 9-mer–containing EC (EC9) after incorporation of seven nts in the presence of adenosine triphosphate (ATP) and uracil triphosphate (UTP) as the only NTP substrates (Fig. 1*A*). An MTase-truncated NS5 (D263) yielded higher-solubility EC9 that was successfully crystallized for determination of a 2.85-Å resolution structure by molecular replacement (MR) (Fig. 1*B* and Table 1). A 2.58-Å precatalysis cytosine triphosphate (CTP) complex structure was also obtained via soaking trials with native EC crystals soaked in low concentration of magnesium ion (0.1 mM) for a short duration (10 min) (Table 1). For both structures, six ECs are present in the crystallographic asymmetric unit of the $P2_1$ lattice. The protein conformation is highly consistent in both structures, with rmsd values of superimposable α-carbon atoms in the range of 0.3 to 0.5 Å (chain M of the native structure as reference, 97 to 100% residue coverage). The RNA conformation is also largely consistent with variations mostly observed at both the upstream and downstream ends. Variations at the upstream are around positions −7 to −9 of the product strand. In the native EC complex, the downstream stem-loop is disordered, while in the CTP complex, the electron density of part of the stem-loop is visible with a maximum of 3 bps resolved including a G:A mismatch (Fig. 1*C*).

Two modes of global conformations have been observed in full-length flavivirus NS5 structures. A fully ordered and properly folded mode represented by the JEV NS5 structure (JEV-mode) features a hydrophobic interaction network in the MTase–RdRP interface involving the RdRP ring finger tip (13, 19). The other mode is represented by a DENV serotype 3 NS5 structure (DENV3-mode) with part of the index, ring, and pinkie finger subdomains disordered (15, 19). Except for the PE substructure, the RdRP conformation of the EC structures is highly consistent with the JEV-mode (rmsd = 1.1 Å, chain M of the native EC structure as reference, residue coverage = 97%), supporting our earlier proposal of the JEV-mode conformation being relevant to RdRP synthesis (19). As anticipated, the PE, observed as an extended loop in apo NS5 structures, retreats from the active site and refolds as a β-hairpin–containing substructure near the top of the thumb, forming interactions with both strands of the upstream RNA duplex (Fig. 1 *B* and *D*). In the study reporting the HCV IC, an RdRP structure with a 5-base pair (bp) upstream duplex was also reported (11). However, the PE_N that plays a critical role at initiation is truncated for eight residues in obtaining such a template–primer complex, and no specific interactions were observed between the truncated PE_N and RNA, and no refolding of the truncated PE_N was observed between the complex structure and corresponding apo structure (Fig. 1*E*).

Structural Basis of the Transition to Elongation in DENV2 RdRP. The DENV2 RdRP PE comprises residues 785 to 807, and in its EC conformation, the N-terminal two-thirds refolds into a β-hairpin (786 to 798) with its flanking regions connecting to two thumb domain helices (Fig. 2*A*). Residues W803 and M804 near the C-terminal end of the PE and residues V788 and H798 of the β-hairpin form an array of hydrophobic–polar interactions with the backbone of the template RNA at positions −7 and −8 (Fig. 2 *B*, *Left*). The peptide backbone of residues T790–S791–R792 near the tip of the β-hairpin established hydrophobic interactions with the backbone of positions −5 and −6 of the product RNA, while the side chain guanidinium of R792 forms electrostatic interactions with the phosphate of −5 product nucleotide (Fig. 2 *B*, *Right*). The RNA sequence–independent interactions of the EC-mode PE indicate that it may act as a processivity factor in the RdRP elongation phase. This observation is reminiscent of the coronavirus (CoV) nsp8 interaction with the upstream RNA duplex backbone between positions −15 and −29 in the RdRP complex with long RNA constructs that enhances complex stability, with each of the two nsp8 molecules interacting with both RNA strands (21–23). By comparing PE conformations in the apo DENV/JEV structures and in the EC, the conformational change during the transition toward elongation can be described as a lift of the product side of the apo conformation loop over its template side (Fig. 2*C*). Residue H798 at the tip of the loop moves over 30 Å to reside at the distal end of the EC β-hairpin, highlighting the scale of PE refolding. Among the three PE tryptophan residues invariant in flaviviruses (Fig. 2*D*), W787 almost maintains its position near the top of the thumb; W803 moves about 12 Å concurrent with the lengthening of the C-terminal thumb helix, and the putative key initiation residue W795 moves about 23 Å to stack on top of W787 and reside at the middle of the EC β-hairpin. R792 that forms stacking interactions with W795 in the apo conformation moves about 8 Å to become the tip of the EC β-hairpin (Fig. 2*C*).

PE Plays Essential Roles at Both Initiation and Elongation. In order to further dissect the function of PE, we designed a series of mutations mainly based on the DENV2 RdRP EC structures and at flavivirus invariant/highly conserved PE sites. Residues R792, H798, W803, and M804 that have side chain contacts with the EC upstream RNA duplex and W795 that plays functional roles at initiation and structural roles at elongation were chosen for comparative analyses with the wild-type (WT) enzyme in the full-length NS5 context (Fig. 2*D*). T790 and S791 coordinate with R792 for product RNA interaction, but they were not chosen for mutation as only their peptide backbone interacts

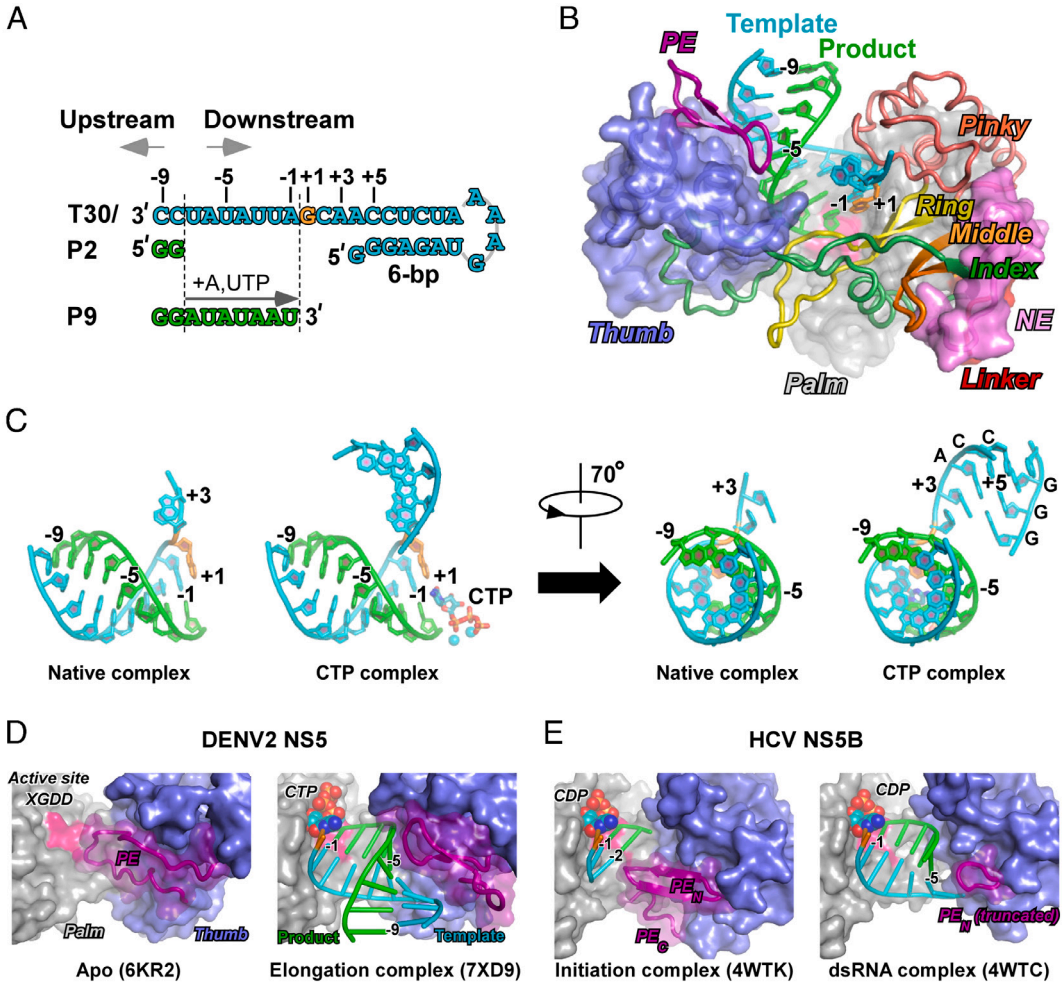

Fig. 1. Crystal structures of DENV2 NS5 EC reveal PE refolding upon transition to elongation. (*A*) The T30/P2 RNA construct used for EC assembly, and the 9-nt product (P9) formed during the assembly. (*B*) Global view of the native EC as a combination of surface and cartoon representations. (*C*) Nucleic acids resolved in EC structures. CTP and magnesium ions are shown as sticks and cyan spheres respectively. (*D*) A comparison of PE conformation in apo DENV2 NS5 (*Left*) and EC–CTP (*Right*) structures. For clarity, the RdRP fingers domain and RNA downstream of +1 are not shown. PE is shown as a combination of cartoon and semitransparent surface representations. CTP is shown as spheres. (*E*) HCV RdRP–RNA complex structures for comparison. *Left*: HCV IC structure obtained using a dinucleotide primer and an NDP; *Right*: template–primer–NDP structure obtained using HCV RdRP with a truncated PE_N. Coloring scheme: palm, gray; thumb, slate; index, dark green; middle, orange; ring, yellow; pinkie, pink; PE, purple; active site XGDD residues, magenta; template, cyan (+1 nucleotide in orange); and product, green. HCV structures were superimposed to DENV2 NS5 EC structure by the traditional least-square method using RdRP motif C as the target region and were shown as separated structures.

with RNA. Among the template RNA–interacting residues, V788 has a longer interacting distance than W803 and M804 (greater than 4 Å vs. about 3 Å) and therefore was not chosen for mutation. Using dinucleotide-driven RdRP assays established in our previous studies and also used in EC assembly and structure determination, RdRP initiation was assessed via a combination of two assay types (Fig. 3*A*). First, multiple-turnover conversion of the dinucleotide P2 to trinucleotide P3 in the presence of 600 μM ATP was monitored. Second, single-turnover conversion of P2 to 9-nt product (P9) under 100 μM UTP and 300 or 1,000 μM ATP was assessed. While the P2-to-P3 assay provides an initial evaluation of initiation efficiency, the P2-to-P9 assay largely rules out the contribution of RdRP complex instability to the initiation kinetics owing to the completion of transition to elongation upon P9 synthesis (19). The data from these two assays together suggest that W803A, W803H, and M804K are more efficient in initiation than the WT enzyme, with about 3- to 5-fold P2-to-P9 conversion rate and 3- to 3.5-fold P2-to-P3 conversion rate at the shortest reaction time point, at which P2 was nearly depleted for fast-initiating mutants (Fig. 3 *B* and *C*). Somewhat surprisingly, W795, H798, and R792 that may directly and indirectly participate in initiation nucleotides contacts exhibit WT-level initiation kinetics. It is likely that initiation efficiency is controlled by multiple factors including PE positioning as an initiation platform and PE structural stability and dynamics. Located at the product/NTP side of the initiation-mode PE, residues 803 and 804 both containing large hydrophobic side chains may be susceptible to mutations in modulating RdRP initiation.

Of particular interest is the effect on EC properties brought by PE mutations. In order to characterize the rapid synthesis of RdRP elongation, we established a single-nucleotide elongation assay by converting the P9 in EC9 to P10 using a quench-flow instrument (Fig. 3*D*). The assay was carried out at 25 °C under saturating NTP concentration (300 μM) and relatively high concentration of NaCl to improve EC9 solubility. It turned out that all PE mutants tested exhibited similar elongation rate about 7 to 11 $nt{\cdot}s^{-1}$ and is comparable with the WT level of 7.8 $nt{\cdot}s^{-1}$ (Fig. 3*E*). The deletion of MTase (i.e., the D263 construct) does not affect elongation rate (8.2 $nt{\cdot}s^{-1}$), while mutation of the NTP ribose–binding motif B serine to threonine (S601T) greatly reduced the rate (1.2 $nt{\cdot}s^{-1}$). These data suggest that PE interactions with the upstream RNA duplex at elongation may not regulate the

Table 1. X-ray diffraction data collection and structure refinement statistics

Crystal form—PDB	7XD8—(Native)	7XD9—(CTP)
Data collection*		
Space group	$P2_1$	$P2_1$
Cell dimensions		
a, *b*, *c* (Å)	141.7, 156.3, 174.4	139.4, 154.6, 172.4
α, β, γ (°)	90, 94.2, 90	90, 94.7, 90
Resolution (Å)†	50.0–2.85 (2.95–2.85)	50.0–2.58 (2.67–2.58)
R_{merge}	0.091 (0.73)	0.044 (0.50)
R_{meas}	0.104 (0.84)	0.052 (0.59)
$CC_{1/2}$	0.991 (0.742)	0.996 (0.806)
I/σI	13.9 (1.8)	23.8 (2.5)
Completeness (%)	87.9 (90.9)	99.8 (99.8)
Redundancy	4.0 (3.9)	3.3 (3.2)
Refinement		
Resolution (Å)	2.85	2.58
No. of unique reflections	154,665	227,687
R_{work}/R_{free}‡ (%)	19.9/24.3	19.1/22.1
No. of atoms		
Protein/RNA	28,661/2,609	29,182/2,932
Ligand/ion	30/12	246/24
Water	177	494
B-factors (Å†)		
Protein/RNA	73.4/69.9	64.8/63.5
Ligand/ion/water	62.0/68.4/59.2	67.6/71.7/67.6
RMS deviations		
Bond lengths (Å)	0.008	0.008
Bond angles (°)	1.062	1.052
Ramachandran statistics§	88.9/10.6/0.2/0.2	89.8/9.8/0.1/0.4

*One crystal was used for data collection for each structure.
†Values in parentheses are for the highest-resolution shell.
‡5% of data are taken for the R_{free} set.
§Values are in percentage and are for most favored, additionally allowed, generously allowed, and disallowed regions in Ramachandran plots, respectively.

chemistry step of nucleotide addition cycle. Moreover, unlike what was in our previous study illustrating the contribution of MTase–RdRP interaction in RdRP initiation (19), the MTase may have a minimum role at elongation as we previously proposed (24). We next assessed EC stability using an established challenge-and-chase type of assay under relatively stringent condition of 30 °C and 525 mM NaCl. Under this condition, WT enzyme has a dissociation/inactivation rate constant (k_{ina}) of $2.6 \times 10^{-3} \cdot h^{-1}$ (corresponding to an EC half-life of longer than 200 h) (Fig. 3*E*). Except for H798A that has WT-level EC stability, all other PE mutants exhibited lower stability at 2- to 90-fold of the WT level (corresponding to an EC half-life of 3 to 108 h), indicating that PE plays an important role in stabilizing RdRP EC likely through its interactions with the upstream RNA duplex. It is worth noting that W803A, W803H, and M804K that exhibit fast initiation feature all have apparently impaired EC stability (corresponding to changes about 15 to 90 fold). The apparent impairment of EC stability by the W795A mutation (a 25-fold change) suggests that the structural stability of the refolded PE is another contributor to PE stabilization of EC as the establishment of stacking interactions between the large aromatic side chains of W795 and W787 could be essential to maintain the EC-mode PE fold (Fig. 2*C*).

Critical Transition toward Elongation Occurs after Synthesis of a 4- to 5-nt product. The observation of apo (presumably similar to IC) and EC conformations of PE sets the stage to investigate the entire transition from initiation to elongation. In order to better understand the intermediate stages of the transition, we compared single-nucleotide initiation and P9 formation using di-(P2), tri-(P3), tetra-(P4), penta-(P5), and septa-(P7) nucleotides as primers (*SI Appendix*, Fig. S1*A*) in both DENV2 and HCV RdRPs. Given equal molar amount of primers, the primer consumption in the single-nucleotide initiation diminished with an increase of primer length (*SI Appendix*, Fig. S1 *B* and *C*, compare lanes 3 to 5, 6 to 8, 9 to 11, 24 to 26, and 27 to 29 for DENV2 and compare lanes 43 to 45, 46 to 48, 49 to 51, 64 to 66, and 67 to 69 for HCV). As discussed earlier, the accumulation of the product may be related not only to catalytic efficiency but also to the stability of the RdRP complex. In this case, complex with different product length may indeed have distinct stability. Therefore, the formation of P9 is a better assessment of initiation efficiency. It turned out that P9 formation from P2 and P3 has comparable kinetics and is apparently faster than that from P4, P5, and P7 in DENV2 RdRP (*SI Appendix*, Fig. S1*B*, lanes 12 to 17 vs. lanes 18 to 20 and 30 to 35), while in HCV, a similar trend was observed but with P4-to-P9 conversion only moderately slower than P2/P3-to-P9 conversion (*SI Appendix*, Fig. S1*C*, lanes 52 to 57 vs. lanes 58 to 60). These data suggest that the key conformational changes of PE toward its EC fold may occur at least after tetranucleotide formation. Moreover, the appearance of 5- to 8-mer intermediate products (indicated by solid triangles in lanes 20, 32 to 35, 72, and 75 of *SI Appendix*, Fig. S1 *B* and *C*) in the P4/P5/P7-driven conversion to P9 in DENV2 and the P5/P7-driven conversion to P9 in HCV also suggests that the transition to elongation may be impaired by starting with these relatively long primers.

Because initiation from longer primers (P3 to P7) does not necessarily well mimic a P2-derived complex stalling at corresponding positions. Similarly, subsequent synthesis from these primers may not have the same behavior as that observed in P2-driven assays. We therefore designed a T28/P2 construct and combined it with T30-7/P2 to qualitatively assess P2-derived complex stability with product length of 4, 5, or 7 nt (Fig. 4*A*). For both DENV2 NS5 and HCV NS5B, P2-to-P4 conversion exhibited multiple-turnover behavior, suggesting that synthesis of both enzymes is still in the initiation phase (Fig. 4*B*, lanes 2 to 10 and 32 to 40). 3-mer intermediate products and 5-mer misincorporation-derived products were observed in both enzyme systems and are more prominent in HCV NS5B. For P2-to-P5 conversion, DENV2 NS5 clearly exhibited a single-turnover behavior similar to that observed in P2-to-P9 conversion assays, suggesting it has largely made the transition to the elongation phase (Fig. 4*B*, lanes 11 to 19). By contrast, although the accumulation of 5-mer slowed down in HCV NS5B, it still exhibited multiple-turnover feature, suggesting that the HCV enzyme has not yet completed the transition (Fig. 4*B*, compare lanes 41 to 49, 11 to 19, and 32 to 40). For P2-to-P7 conversion, single-turnover behavior was observed for both enzymes (Fig. 4*B*, lanes 22 to 30 and 51 to 59). Despite different nature of the assays discussed above, these data suggest the same timing for critical transition for both enzyme systems after the synthesis of a 4- to 5-nt product (Fig. 4*C*, a model for DENV2 NS5).

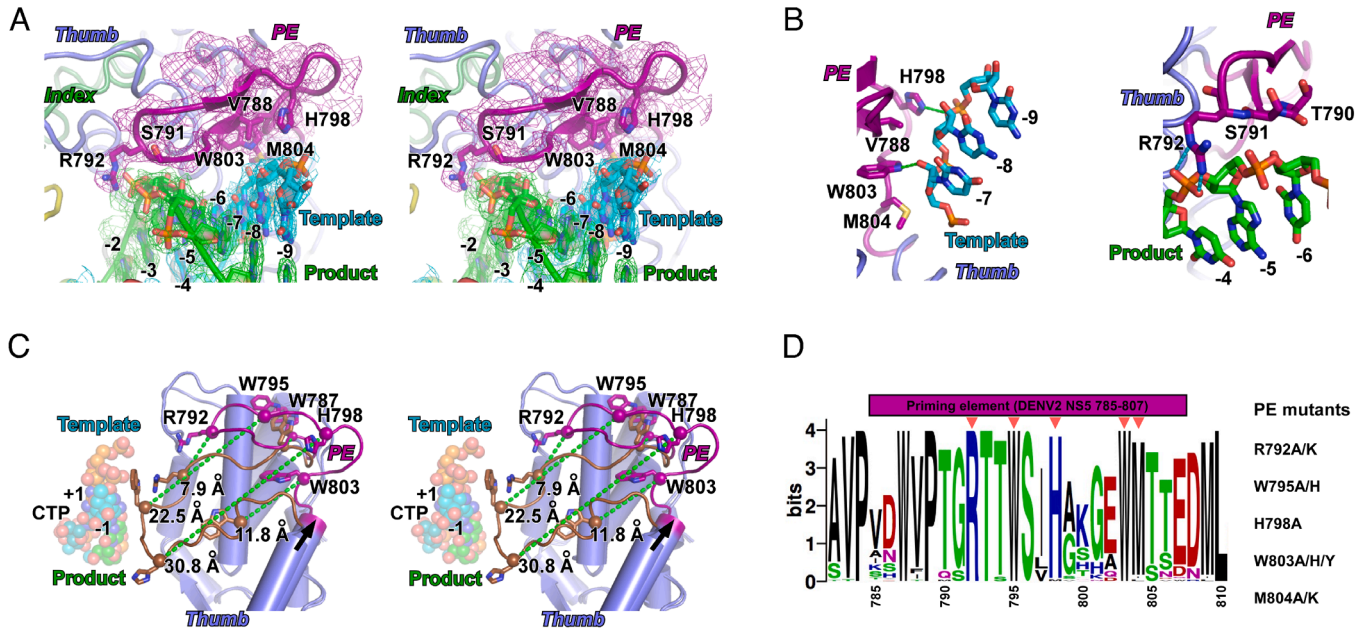

Fig. 2. The details of PE interactions with the upstream RNA duplex in EC and its refolding from apo state to elongation state. (*A*) Stereopair images of PE interactions with the upstream RNA duplex. EC–CTP complex structure is shown as cartoon representations and with 3,500-K simulated-annealing omit $2F_o–F_c$ electron density maps overlaid (contoured at 1.2 σ). Side chains of key PE residues involved in RNA contacts are shown as sticks. (*B*) PE–RNA backbone interactions with the −7/−8 positions of the template (*Left*) and the −5/−6 positions of the product (*Right*). (*C*) Stereopair images for an illustration of PE refolding using the apo JEV NS5 (brown PE) and DENV2 NS5 EC–CTP (purple PE) structures. The JEV structure is used because it has relatively intact side chain models if compared with DENV2 apo structures. The α-carbon atoms of four hallmark residues (large spheres) and a reference residue (small spheres) are shown with the corresponding moving distances for illustration of the refolding scheme. Initiating nucleotides were modeled from the EC–CTP structure and are shown as semitransparent spheres. (*D*) Structure-based PE mutation design. *Left*: sequence logos generated using a multiple-sequence alignment of NS5 sequences from 45 flaviviruses (http://weblogo.berkeley.edu/) to show conservative levels of PE residues. Mutation sites were indicated by red triangles. *Right*: A list of 10 PE mutations designed. Coloring scheme in panels *A*–*C* is the same as in Fig. 1.

Discussion

The observation of DENV2 RdRP PE refolding and its bifunctional feature both at initiation and elongation evokes us to propose that classical de novo RdRPs may share a common mechanism in utilizing their PEs in spite of diversity in both sequence and structure (*SI Appendix*, Fig. S2 and Fig. 5*A*). In the absence of RNA template and initiation NTPs/short primers, PE conformations may vary (Fig. 5*A*, JEV and CSFV structures). Upon template and NTP/primer binding, PE stacks on the upstream end of the initiation nucleotides, and an induced-fit mechanism may need to occur starting from the corresponding apo conformation (17) (Fig. 5*A*, HCV and phi6 structures). The lengthening of the template–product duplex may induce incremental conformational changes initially while retaining the PE upstream RNA interactions (Fig. 4*C*, first three models). At some point during the transition toward elongation, refolding or more abrupt conformational changes may occur, and PE switches to its elongation-mode conformation (Fig. 4*C*, from the third model to the fourth). Further lengthening of the RNA duplex helps finalize EC-mode contacts between PE and backbone of the upstream RNA duplex, which are essential for EC stability (Fig. 4*C*, last three models). This working model is different from what was suggested in influenza viruses of the negative-strand RNA viruses, where their RdRP PE (termed priming loop) may play similar roles at initiation as in classical de novo RdRPs, and the lengthening of the template–product RNA duplex resulted in an extrusion of PE from the duplex-binding channel and becomes largely disordered at elongation (25). Solving more classical de novo RdRP EC structures, such as those of HCV, CSFV, and phi6, will help improve the understanding of the common theme of the transition suggested in this work.

Similar to other positive-strand RNA viruses, the *Flaviviridae* members have their replication–transcription complex (RTC) assembled around RdRP in membrane-associated microstructures in the cytoplasm (26, 27). Other nonstructural proteins may participate in the RTC, in particular for NS3 protein that possesses both helicase and protease functions (28–30). NS3 is known to cooperate with RdRP (either NS5 or NS5B in different *Flaviviridae* genera) (31–33). However, the details of its interaction with RdRP and the precise mechanism both remain elusive. The PE refolding upon transition to elongation observed in DENV2 RdRP demonstrates that an actively synthesizing RdRP can undergo conformational change to alter its surface properties. This feature on one hand can bring complications to the interactions between RTC components and on the other hand may provide routes to assemble RTC-related complexes for structural and functional studies to dissect RTC working mechanisms, in particular for RdRP crosstalk with other components such as NS3. On the antiviral front, conformational change of PE and its consequence in alteration of RTC component interaction could provide target site(s) for intervention.

The contribution of DENV2 RdRP PE at elongation may be surprising since this type of substructure was only known for critical contribution at polymerase initiation. On the other hand, the switch of function at elongation demonstrates efficient usage of PE, in particular for relatively compact classical de novo RdRPs typically not having other proteins or intramolecular modules to help improve the stability of EC. While a similar phenomenon has not been found in other viral RdRPs, a somewhat analogous example is present in bacteriophage T7 RNA polymerase, a single-subunit DNA-dependent RNA polymerase. This ~900-residue enzyme contains a β-type substructure named the specificity loop (corresponding to residues 740 to 769) slightly larger than the size

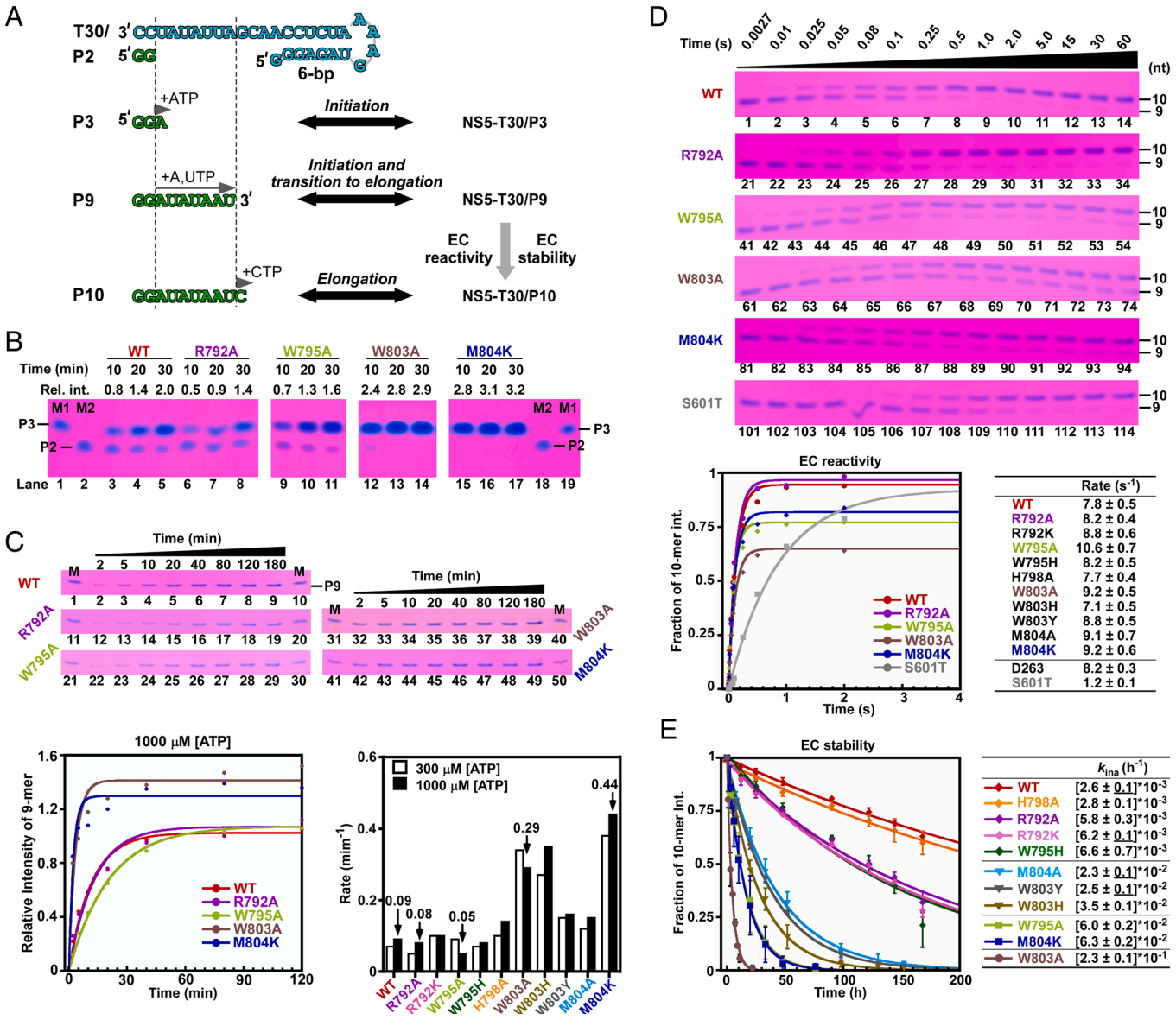

Fig. 3. Enzymology characterizations of DENV2 WT NS5 and its PE mutants. (*A*) Four types of RdRP assays based on the T30/P2 construct were also used for structure determination of EC. Initiation kinetics was assessed by a combination of P2-to-P3 and P2-to-P9 conversions. EC reactivity was assessed by P9-to-P10 conversion rate under high-salt condition (300 mM NaCl) using a quench-flow instrument. EC stability was assessed by P9-to-P10 conversion after an incubation under a challenging condition (525 mM NaCl and 30 °C) for various periods. (*B*) Gel images of representative NS5 constructs for P2-to-P3 conversion. Chemically synthesized P2 and P3 were used as migration markers, and P3 was also used as standard samples (M1 lanes) for relative P3 intensity quantitation. For every separated gel image, there were WT samples loaded (but not shown for the right three images) for quantitation of P3 relative intensities. (*C*) Analysis of P2-to-P9 conversion. *Top*: Gel images of representative NS5 constructs for P2-to-P9 conversion under 1,000 μM ATP concentration. *Bottom Left*: Fitting of conversion rates of P2 to P9 for representative NS5 constructs. *Bottom Right*: Bar chart showing conversion rates of P2 to P9 under two ATP concentrations. Values and arrows above the bars show rates of representative constructs under 1,000 μM ATP concentration. A chemically synthesized 8-mer (sequence not related to P9) was used as a migration marker (M lanes) and as standard samples for relative P9 intensity quantitation. (*D*) EC reactivity assessment by quench-flow kinetics. *Top*: Gel images of representative NS5 constructs for P9-to-P10 conversion. A motif B mutant S601T and the MTase-truncated mutant D263 were used for comparison. *Bottom*: Fitting of conversion rates of P9 to P10 for all NS5 constructs tested. (*E*) EC stability assessment. Fitting of inactivation (dissociation) rate constant (k_{ina}) of EC for all NS5 constructs tested. Underlined fitting errors indicate actual values smaller than 0.1. Error bars in the left panel show SDs of fraction of 10-mer intensity values measured in three individual experimental sets.

of flavivirus RdRP PE. The specificity loop adopts an extended hairpin-like structure and plays essential roles at initiation by sequence-specific interactions with the major groove of the double-stranded (ds) promoter around position −9 (34) (Fig. 5*B*, *Left*), coordinating with the NTD in promoter binding. During the transition toward elongation, the NTD rotates with the promoter to accommodate the growth of the template–product duplex, while the specificity loop moves with the promoter and undergoes moderate conformational changes (35) (Fig. 5 *B*, compare *Left* and *Middle* structures). Upon transition to elongation and loss of promoter contacts, the specificity loop adopts a more compact structure quite similar to the elongation-mode DENV2 RdRP PE and becomes part of the upstream RNA exit tunnel that is also critical to EC stability in T7 RNA polymerase (36–38) (Fig. 5 *B*, *Right*). The major difference in these two refolding events is that DENV2 PE refolding is relatively local, but T7 specificity loop refolding is associated with the movement of the entire NTD. What is also in common in the conformational switching of DENV2 PE and T7 specificity loop is the establishment or change in protein–nucleic acid interactions. With recent breakthrough of protein structure prediction, protein ground-state conformation(s) may be readily accessible to researchers without

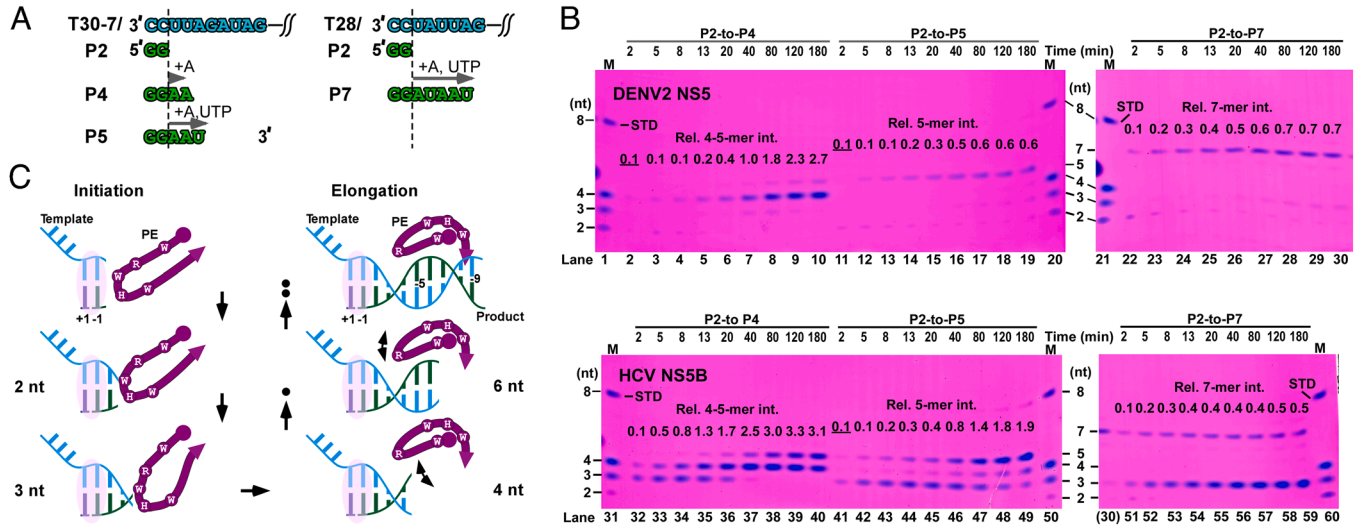

Fig. 4. A working model of the transition toward elongation in classical de novo RdRPs. (*A*) Two RNA constructs used for dissection of transition toward elongation in DENV2 and HCV RdRPs. (*B*) Multiple-nucleotide incorporation assays (P2 to P4 and P2 to P5 for the T30-7/P2 construct and P2 to P7 for the T28/P2 construct) were used to estimate the critical step during transition toward elongation for DENV2 RdRP. Chemically synthesized P2/P3/P4 was used as a migration marker (M lanes). The same 8-mer in Fig. 3*C* was also used as a migration marker (M lanes) and as standard samples (M lane, STD) for relative 4- to 5-mer, 5-mer, and 7-mer intensity quantitation. The P2-to-P7 gel images for DENV2 (*Top*) and HCV (*Bottom*) were cropped from different regions of the same gel, and lane 30 was included in both images for correlation. The STD samples were provided at the same molar amount as the RNA template, and the average intensity of P8 band on both sides of each gel is set to 1.0. Based on Stains-All staining nature, equal molar amount of shorter RNA (e.g., P7, P5, or P4) should have lower band intensity than that of P8 standard. Therefore, the relative intensity values in combination with time course accumulation behavior can help distinguish single- and multiple-turnover synthesis. (C) A working hypothesis of flavivirus RdRP transition from initiation to elongation proposed partly based on EC structures and data in panel *B*. During the early stages of the transition, hydrophobic stacking interactions between the PE and the initiation nucleotides are maintained, while PE undergoes incremental conformational changes to accommodate the lengthening of the upstream RNA duplex (*Left* three models). At some point during the transition (proposed here after formation of a 4-nt product), an abrupt conformational change leads to elongation-mode fold of PE with the loss of its initiation-mode contacts with the RNA (from the third model to the fourth model). Complete establishment of elongation-mode interactions with the upstream RNA duplex may take several nucleotide addition cycles until the duplex length reaches 8 to 9 bps (*Right* three models). Pink ovals indicate the RdRP active site. The filled circle and arrowhead indicate the N-to-C direction of PE peptide segment. Filled circles with capital letters indicate hallmark PE residues (equivalent to those shown in Fig. 2*C*).

experimental determination of the three-dimensional structure (39). However, function-related conformational changes, in particular those driven by protein–nucleic acid interactions, are still challenging. Events like PE refolding may be good learning cases for artificial intelligence technology such as deep learning to solve the puzzle of assembly and dynamics of complicated biological macromolecular complexes in the future.

Materials and Methods

Cloning and Protein Production. The parental plasmid of pET26b-DENV2 NS5 WT was used to produce an N-terminal–truncated mutant (DENV2 NS5_D263; residues 264 to 900) and 10 full-length NS5 constructs with point mutations by using the QuikChange site-directed mutagenesis method as described previously (19, 40). The DENV2 NS5_D263 protein was expressed in *Escherichia coli* strain BL21-Rosetta(DE3), and ten full-length NS5 point mutation constructs were expressed in BL21-CodonPlus(DE3)-RIL with a C-terminal hexahistidine tag. Cells were grown and harvested as previously described (19). The HCV NS5B protein was expressed in *E. coli* strain BL21-Rosetta(DE3) with a C-terminal hexahistidine tag. Cells were grown and harvested as DENV2 NS5 protocols described except that the TB culture medium was used and the induction temperature was 18 °C.

Protein Purification. For DENV2 NS5 and its variants, cell lysis, subsequent purification, and storage procedures were as previously described (19) except that polyethylenimine (PEI) was added slowly to a final concentration of 0.04% (vol./vol.) over a 20-min period to precipitate nucleic acid, and the NaCl concentration of NS5_D263 nickel-affinity fractions needed to be adjusted to 50 mM NaCl before loading onto the HiTrap SP HP column (GE Healthcare). The molar extinction coefficients for the DENV2 NS5 WT and its variants were calculated based on protein sequence using the Expasy ProtParam program (http://www.expasy.ch/tools/protparam.html). The final fractions were concentrated to approximately 20 mg/mL, flash frozen with liquid nitrogen, and stored at −80°C in 5 to 20 μL aliquots, and the yield of pure protein is typically 1.5 to 4 mg/L bacterial culture.

For HCV NS5B, cell lysis, subsequent purification, and storage procedures were the same as DENV2 NS5 protocols except that the PEI precipitation step was omitted, a wash step using a wash buffer containing 100 mM imidazole, 50 mM Tris (pH 7.5), 300 mM NaCl, and 20% (vol./vol.) glycerol was applied prior to the elution step in the nickel-affinity chromatography, the pooled fractions were diluted twofold with an SP low-salt buffer [25 mM 2- (N-morpholino)ethanesulfonic acid (MES) (pH 6.5), 300 mM NaCl, 5% (vol./vol.) glycerol, and 0.1 mM ethylene diamine tetraacetic acid (EDTA)] before loading onto the cation exchange column, and the gel filtration buffer was 5 mM Tris (pH 7.5), 500 mM NaCl, and 5% (vol./vol.) glycerol. The yield of pure protein is typically 12 mg/L bacterial culture.

RNA Preparation. A chemically synthesized (Integrated DNA Technologies, Dharmacon, or an in-house K&A H-8 RNA synthesizer) 30-mer RNA (T30) with a hairpin structure at its 5′-end was used as template for de novo polymerase assays. The RNA was purified by 12% (wt./vol.) polyacrylamide/7M urea gel electrophoresis and stored at −80 °C after a self-annealing process as previously described (40). GG (P2, Jena Bioscience, or Takara Bio) and GGA/GGAU/GGAUA/GGAUAUA (P3/P4/P5/P7; Takara Bio) nucleotides were annealed with template at 5:1 or 20:1 molar ratio by a 3-min incubation at 45 °C followed by slowly cooling to room temperature in RNA annealing buffer of 50 mM NaCl, 5 mM $MgCl_2$, 5 mM Tris (pH 7.5) to make the T30/P2, T30/P3, T30/P4, T30/P5, T30/P7, T30-7/P2, and T28/P2 RNA constructs.

DENV2 NS5_D263 EC Assembly, Purification, and Crystallization. To assemble EC containing the 9-mer product (EC9), DENV2 NS5_D263 protein and the T30/P2 construct were mixed at final concentrations of 24 μM and 20 μM, respectively, in a reaction buffer containing 100 mM N-2-hydroxyethylpiperazine-N-2-ethane sulfonic acid (HEPES) (pH 7.0), 40 mM NaCl, 10 mM $MgCl_2$, and 10 mM dithiothreitol (DTT), and ATP and UTP were provided at a final concentration of 600 μM each. A typical 2-mL EC9 reaction mixture was incubated at 30 °C for about 2 h, and then, NaCl concentration was adjusted to 145 mM by supplementing 5 M NaCl solution. The supernatant of the reaction mixture was then loaded into a

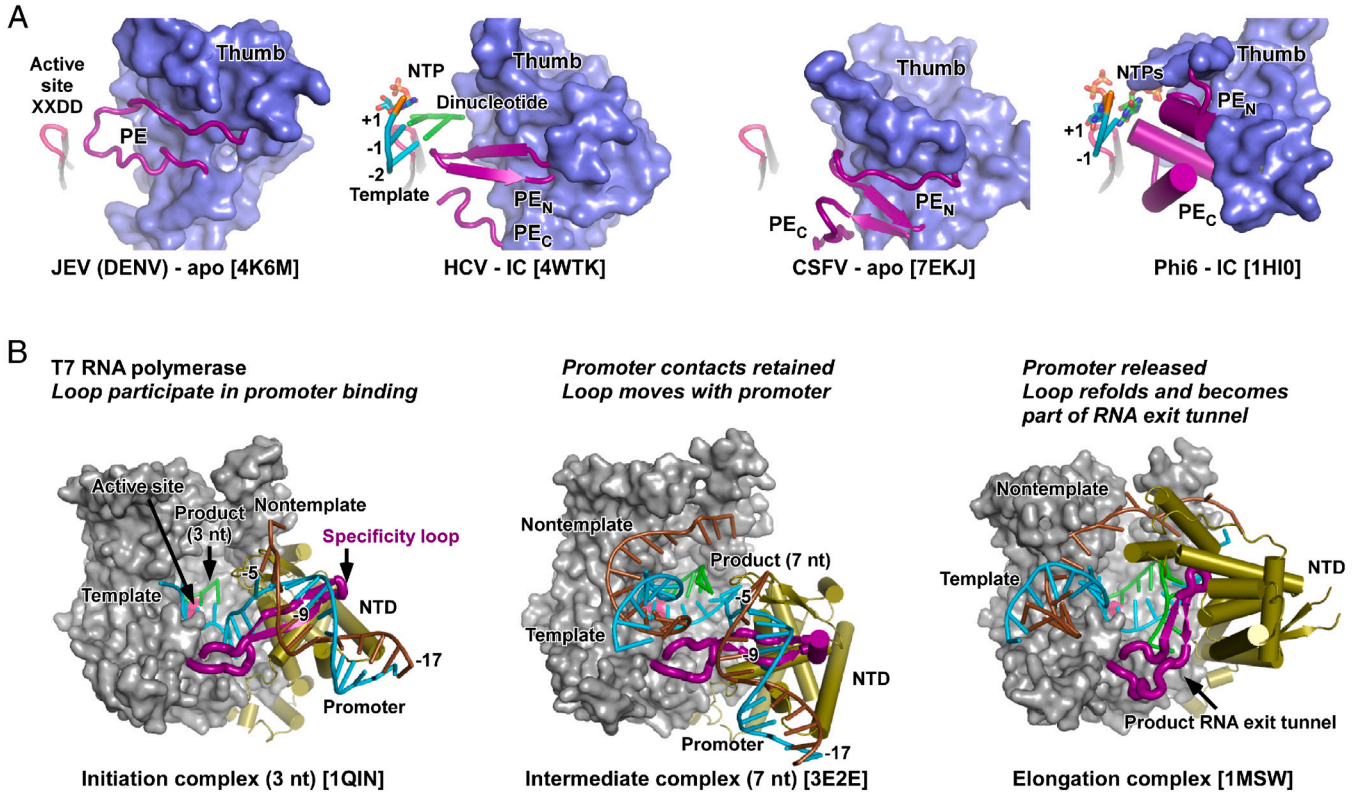

Fig. 5. Structure diversity of de novo RdRP PEs and a structural comparison of DENV2 RdRP PE and T7 RNA polymerase specificity loop in transition toward elongation. (*A*) A structural comparison of representative PEs in classical de novo RdRPs. From *Left* to *Right*, JEV NS5 apo structure, HCV NS5B IC structure, CSFV NS5B apo structure, and phi6 RdRP IC structure. For clarity, only thumb (surface), PE (cartoon), XXDD-containing motif C (cartoon), and initiation nucleotides (cartoon or sticks) are shown. CSFV, HCV, and phi6 structures were superimposed to JEV NS5 apo structure by the traditional least-square method using RdRP motif C as the target region and were shown as separated structures. (*B*) A structural comparison of specificity loop conformations in different stages of T7 RNA polymerase transcription. *Left*: IC structure; *Middle*: structure of an intermediate complex between initiation and elongation; and *Right*: EC structure. The polymerase core module is shown as surface representations; the specificity loop, NTD, and nucleic acids are shown as cartoon representations. Coloring scheme: polymerase core, gray; NTD, olive; specificity loop, purple; template, cyan; product, green; and nontemplate, brown. Position labels in panel *B* correspond to positions relative to transcription start site.

Mono Q column (GE Healthcare) equilibrated in a low-salt buffer [50 mM HEPES (pH 7.0), 120 mM NaCl, 5 mM $MgCl_2$, and 5 mM DTT], and the EC9 sample was eluted with a linear gradient to 1 M NaCl, buffer-exchanged into a storage buffer of 50 mM Tris (pH 7.5), 100 mM NaCl, 5 mM $MgCl_2$, and 5 mM tris(2-carboxyethyl) phosphate, and then concentrated to 8 mg/mL or higher for crystallization. The successful EC9 crystals were grown by sitting drop vapor diffusion at 22.5 °C using 7 to 8 mg/mL EC9 sample. With a starting drop volume of 0.6 μL, crystals were grown in 2 to 5 d to their final dimension with a precipitant/well solution containing 2.2 to 2.65 M sodium formate and 10 to 20% (vol./vol.) glycerol prior to flash cooling in liquid nitrogen. For CTP soaking experiments, crystals were soaked in a buffer containing 2.5 M sodium formate, 20% glycerol (vol./vol.), 5 mM CTP, and 0.1 mM $MgCl_2$ for 10 min at 16 °C prior to flash cooling and storage.

Crystallographic Data Processing and Structure Determination. X-ray diffraction data were collected at the Shanghai Synchrotron Radiation Facility (SSRF) beamlines BL19U1 (native EC, wavelength: 0.9785 Å) and BL17U1 (CTP complex, wavelength: 0.9792 Å) at 100 K. Data of 180 to 360° were collected in 0.2 to 0.4° oscillation steps. Reflections were integrated, merged, and scaled using HKL2000 (41). The initial structure solution was obtained using the MR program PHASER (42) using a search model derived from apo protein models of flavivirus NS5 and template–product RNA of an EV71 RdRP EC (13, 19, 43) [Protein Data Bank (PDB) entries 6KR2/4K6M and 5F8G]. Manual model building and structure refinement were done using Coot and PHENIX, respectively (44, 45). The 3,500 K composite simulated-annealing omit $2F_o–F_c$ electron density maps were generated using CNS (46). The atomic coordinates and structure factors for the reported crystal structures have been deposited in the PDB under accession numbers 7XD8 and 7XD9, and all other data are available in the main text or the *SI Appendix*. Unless otherwise indicated, all RdRP superimpositions were done using the maximum likelihood–based structure superpositioning program THESEUS (47).

In Vitro Polymerase Assays. Unless otherwise indicated, all dinucleotide (P2)-driven assays were carried out as described previously (19). The final reaction solution contains 4 μM RNA template and 6 μM WT NS5 (or its variant) in a reaction buffer of 50 mM Tris (pH 7.5), 20 mM NaCl, 5 mM $MgCl_2$, and 5 mM DTT. For the P2-to-P3 conversion assay, ATP was supplied as the only NTP substrate at 600 μM, and T30/P2 molar ratio was 1:20 to achieve multiple turnovers within a reasonable duration. For the P2-to-P9 conversion assay, ATP and UTP were supplied at a final concentration of 300/1,000 and 100 μM, respectively, and the T30/P2 molar ratio was 1:5. For PX (X = 2/3/4/5/7)-to-P(X + 1) conversion, PX-to-P9 conversion, and P2-to-P4/P5/P7 conversion assays, ATP and/or UTP was supplied at a final concentration of 300 μM, and the T30/PX ratio was 1:5.

The procedure and subsequent analysis of stability assessment of EC9 assembled with WT DENV2 NS5 or its variants were described as previously except that the P2-to-P9 reaction mixture was centrifuged at 16,000 g for 10 s at 4 °C; the pellet was resuspended in a modified reaction buffer with 525 mM NaCl, and the resuspension was incubated at 30 °C for various duration (0 to 168 h).

To assess single-nucleotide incorporation rate of EC9, a rapidly mixing/quenching experiment was performed by using a RQF-3 chemical quench-flow instrument (KinTek Corp.). EC9 was generated following the P2-to-P9 assay protocols with elevated enzyme/RNA concentrations (8 μM template and 12 μM NS5), 300 μM ATP, 100 μM UTP (to reduce the level of 10-mer misincorporation product) at 30 °C for 2 h. 5M NaCl was then supplemented to the reaction mixture to reach a final concentration of 300 mM, and the mixture was centrifuged at 16,000 g for 5 min for pellet removal. The volume of 5M NaCl was accounted for experimental settings to ensure the mixture matches the non-NaCl contents of the reaction buffer. The supernatant was then loaded into the quench-flow instrument where equal volume of EC9-containing sample and 600 μM CTP in a reaction buffer with NaCl concentration elevated to 300 mM were rapidly mixed and then quenched at time points in the range of 0.0027 to 60 s by a stop

solution of 95% (vol./vol.) formamide, 20 mM EDTA (pH 8.0), and 0.02% (wt./vol.) bromophenol blue.

Denaturing polyacrylamide gel electrophoresis analysis to resolve the RNA species, gel staining, band quantitation, and curve fitting of P9 formation were carried out as previously described (19). To estimate the single-nucleotide elongation rate (r) corresponding to P9-to-P10 conversion, the values representing the fraction of 10-mer intensity (f) at all time points (t) were fitted to a single-exponential rise equation: $f = \text{amplitude}[1 - \exp(r \cdot t)]$, where the amplitude considered the possibility of a 9-mer RNA that eventually failed to extend to a 10-mer.

Data, Materials, and Software Availability. Structure factors and coordinates data have been deposited at the Protein Data Bank (PDB, https://www.rcsb.org) under accession codes 7XD8 and 7XD9. All study data are included in the article and/or *SI Appendix*.

ACKNOWLEDGMENTS. We thank Dr. Olve Peersen for recommendation of the HCV EC enzymology work as a basis for EC structure exploration in the early phase of our efforts toward *Flaviviridae* RdRP EC structures and for providing the plasmids for HCV NS5B expression, Dr. Pei-Yong Shi and Dr. Bo Zhang for providing the cloning material for DENV2 NS5 gene, Dr. Weichi Liu, Dr. Linfei Huang, Dr. Peng Bi, and Liu Deng for their efforts in parallel projects in *Flaviviridae* RdRP EC structures, Dr. Hengxia Jia, Shunli Liu, and Xin Wen for laboratory assistance and helpful discussion, Xiang Fang and Dr. Hengxia Jia for help in synchrotron data collection and synchrotron SSRF (beamlines BL17U1/BL02U1 and BL19U1, Shanghai, China) for access to beamlines, and Institutional Center for Shared Technologies and Facilities and Wuhan Institute of Virology for access to instruments. Funding: This study was supported by the National Key Research and Development Program of China (2018YFA0507200 to P.G. and G.L.); the National Natural Science Foundation of China (32070185 to P.G. and 32000136 to J.W.); the Chinese Academy of Sciences Funds: Youth Innovation Promotion Association Program (2022341 to J.W.); Special Research Assistant Program (2021000041 to J.W.), and Advanced Customer Cultivation Project of Wuhan National Biosafety Laboratory (2021ACCP-MS10 to P.G.); and Hubei Province Funds: Key Biosafety Science and Technology Program of Hubei Jiangxia Laboratory (JXBS001 to P.G.) and Young Talent Program of Health Commission (WJ2021Q055 to J.W.).

Author affiliations: [a]Key Laboratory of Special Pathogens and Biosafety, Center for Biosafety Mega-Science, Wuhan Institute of Virology, Chinese Academy of Sciences, Wuhan, Hubei 430071, China; [b]University of Chinese Academy of Sciences, Beijing 100049, China; [c]Drug Discovery Center for Infectious Diseases, Nankai University, Tianjin 300350, China; and [d]Hubei Jiangxia Laboratory, Wuhan, Hubei 430207, China

1. Y. I. Wolf *et al.*, Origins and evolution of the global RNA virome. *mBio* **9**, e02329–18 (2018).
2. P. Gong, Structural basis of viral RNA-dependent RNA polymerase nucleotide addition cycle in picornaviruses. *Enzymes* **49**, 215–233 (2021).
3. J. L. Hansen, A. M. Long, S. C. Schultz, Structure of the RNA-dependent RNA polymerase of poliovirus. *Structure* **5**, 1109–1122 (1997).
4. C. A. Lesburg *et al.*, Crystal structure of the RNA-dependent RNA polymerase from hepatitis C virus reveals a fully encircled active site. *Nat. Struct. Biol.* **6**, 937–943 (1999).
5. P. Gong, O. B. Peersen, Structural basis for active site closure by the poliovirus RNA-dependent RNA polymerase. *Proc. Natl. Acad. Sci. U.S.A.* **107**, 22505–22510 (2010).
6. Y. W. Yin, T. A. Steitz, The structural mechanism of translocation and helicase activity in T7 RNA polymerase. *Cell* **116**, 393–404 (2004).
7. H. Huang, R. Chopra, G. L. Verdine, S. C. Harrison, Structure of a covalently trapped catalytic complex of HIV-1 reverse transcriptase: Implications for drug resistance. *Science* **282**, 1669–1675 (1998).
8. Y. Li, S. Korolev, G. Waksman, Crystal structures of open and closed forms of binary and ternary complexes of the large fragment of Thermus aquaticus DNA polymerase I: Structural basis for nucleotide incorporation. *EMBO J.* **17**, 7514–7525 (1998).
9. C. C. Kao, A. M. Del Vecchio, W. Zhong, De novo initiation of RNA synthesis by a recombinant flaviviridae RNA-dependent RNA polymerase. *Virology* **253**, 1–7 (1999).
10. S. J. Butcher, J. M. Grimes, E. V. Makeyev, D. H. Bamford, D. I. Stuart, A mechanism for initiating RNA-dependent RNA polymerization. *Nature* **410**, 235–240 (2001).
11. T. C. Appleby *et al.*, Viral replication. Structural basis for RNA replication by the hepatitis C virus polymerase. *Science* **347**, 771–775 (2015).
12. K. H. Choi *et al.*, The structure of the RNA-dependent RNA polymerase from bovine viral diarrhea virus establishes the role of GTP in de novo initiation. *Proc. Natl. Acad. Sci. U.S.A.* **101**, 4425–4430 (2004).
13. G. Lu, P. Gong, Crystal structure of the full-length Japanese encephalitis virus NS5 reveals a conserved methyltransferase-polymerase interface. *PLoS Pathog.* **9**, e1003549 (2013).
14. W. Liu, X. Shi, P. Gong, A unique intra-molecular fidelity-modulating mechanism identified in a viral RNA-dependent RNA polymerase. *Nucleic Acids Res.* **46**, 10840–10854 (2018).
15. Y. Zhao *et al.*, A crystal structure of the Dengue virus NS5 protein reveals a novel inter-domain interface essential for protein flexibility and virus replication. *PLoS Pathog.* **11**, e1004682 (2015).
16. W. Li, B. Wu, W. A. Soca, L. An, Crystal structure of classical swine fever virus NS5B reveals a novel N-terminal domain. *J. Virol.* **92**, e00324-18 (2018).
17. B. Y. Zhang, W. Liu, H. Jia, G. Lu, P. Gong, An induced-fit de novo initiation mechanism suggested by a pestivirus RNA-dependent RNA polymerase. *Nucleic Acids Res.* **49**, 8811–8821 (2021).
18. Z. Jin, V. Leveque, H. Ma, K. A. Johnson, K. Klumpp, Assembly, purification, and pre-steady-state kinetic analysis of active RNA-dependent RNA polymerase elongation complex. *J. Biol. Chem.* **287**, 10674–10683 (2012).
19. J. Wu *et al.*, A conformation-based intra-molecular initiation factor identified in the flavivirus RNA-dependent RNA polymerase. *PLoS Pathog.* **16**, e1008484 (2020).
20. P. Gong, M. G. Kortus, J. C. Nix, R. E. Davis, O. B. Peersen, Structures of coxsackievirus, rhinovirus, and poliovirus polymerase elongation complexes solved by engineering RNA mediated crystal contacts. *PloS One* **8**, e60272 (2013).
21. H. S. Hillen *et al.*, Structure of replicating SARS-CoV-2 polymerase. *Nature* **584**, 154–156 (2020).
22. Q. Wang *et al.*, Structural basis for RNA replication by the SARS-CoV-2 polymerase. *Cell* **182**, 417–428 e413 (2020).
23. J. Wu *et al.*, Remdesivir overcomes the S861 roadblock in SARS-CoV-2 polymerase elongation complex. *Cell Rep.* **37**, 109882 (2021).
24. G. Lu, P. Gong, Natural polymerase fusion as an initiation regulator? *Oncotarget* **7**, 35498–35499 (2016).
25. T. Kouba, P. Drncova, S. Cusack, Structural snapshots of actively transcribing influenza polymerase. *Nat. Struct. Mol. Biol.* **26**, 460–470 (2019).
26. I. Romero-Brey, R. Bartenschlager, Endoplasmic reticulum: The favorite intracellular niche for viral replication and assembly. *Viruses* **8**, E160 (2016).
27. T. J. Chambers, C. S. Hahn, R. Galler, C. M. Rice, Flavivirus genome organization, expression, and replication. *Annu. Rev. Microbiol.* **44**, 649–688 (1990).
28. D. Luo *et al.*, Crystal structure of the NS3 protease-helicase from dengue virus. *J. Virol.* **82**, 173–183 (2008).
29. F. Zheng, G. Lu, L. Li, P. Gong, Z. Pan, Uncoupling of protease trans-cleavage and helicase activities in pestivirus NS3. *J. Virol.* **91**, e01094-17 (2017).
30. J. L. Kim *et al.*, Crystal structure of the hepatitis C virus NS3 protease domain complexed with a synthetic NS4A cofactor peptide. *Cell* **87**, 343–355 (1996).
31. M. Y. Tay *et al.*, The C-terminal 50 amino acid residues of dengue NS3 protein are important for NS3-NS5 interaction and viral replication. *J. Biol. Chem.* **290**, 2379–2394 (2015).
32. Y. Wang *et al.*, Characterisation of interaction between NS3 and NS5B protein of classical swine fever virus by deletion of terminal sequences of NS5B. *Virus Res.* **156**, 98–106 (2011).
33. S. Ishido, T. Fujita, H. Hotta, Complex formation of NS5B with NS3 and NS4A proteins of hepatitis C virus. *Biochem. Biophys. Res. Commun.* **244**, 35–40 (1998).
34. G. M. Cheetham, T. A. Steitz, Structure of a transcribing T7 RNA polymerase initiation complex. *Science* **286**, 2305–2309 (1999).
35. K. J. Durniak, S. Bailey, T. A. Steitz, The structure of a transcribing T7 RNA polymerase in transition from initiation to elongation. *Science* **322**, 553–557 (2008).
36. Y. W. Yin, T. A. Steitz, Structural basis for the transition from initiation to elongation transcription in T7 RNA polymerase. *Science* **298**, 1387–1395 (2002).
37. T. H. Tahirov *et al.*, Structure of a T7 RNA polymerase elongation complex at 2.9 A resolution. *Nature* **420**, 43–50 (2002).
38. K. Theis, P. Gong, C. T. Martin, Topological and conformational analysis of the initiation and elongation complex of t7 RNA polymerase suggests a new twist. *Biochemistry* **43**, 12709–12715 (2004).
39. K. Tunyasuvunakool *et al.*, Highly accurate protein structure prediction for the human proteome. *Nature* **596**, 590–596 (2021).
40. J. Wu, G. Lu, B. Zhang, P. Gong, Perturbation in the conserved methyltransferase-polymerase interface of flavivirus NS5 differentially affects polymerase initiation and elongation. *J. Virol.* **89**, 249–261 (2015).
41. Z. Otwinowski, W. Minor, Processing of X-ray diffraction data collected in oscillation mode. *Methods Enzymol.* **276**, 307–326 (1997).
42. A. J. McCoy *et al.*, Phaser crystallographic software. *J. Appl. Crystallogr.* **40**, 658–674 (2007).
43. B. Shu, P. Gong, Structural basis of viral RNA-dependent RNA polymerase catalysis and translocation. *Proc. Natl. Acad. Sci. U.S.A.* **113**, E4005–4014 (2016).
44. P. Emsley, B. Lohkamp, W. G. Scott, K. Cowtan, Features and development of Coot. *Acta Crystallogr. D Biol. Crystallogr.* **66**, 486–501 (2010).
45. P. D. Adams *et al.*, PHENIX: A comprehensive Python-based system for macromolecular structure solution. *Acta crystallogr. D Biol. Crystallogr.* **66**, 213–221 (2010).
46. A. T. Brunger *et al.*, Crystallography & NMR system: A new software suite for macromolecular structure determination. *Acta Crystallogr. D Biol. Crystallogr.* **54**, 905–921 (1998).
47. D. L. Theobald, D. S. Wuttke, THESEUS: Maximum likelihood superpositioning and analysis of macromolecular structures. *Bioinformatics* **22**, 2171–2172 (2006).